Supporting Information

Synergistic 2D Structure Design and High-Entropy Engineering in MnFeCoNiCu Nanoalloy/Carbon Nanosheet Composite to Optimize Impedance Matching for High-Attenuation Microwave Absorption

Xueyang Wang[a,b,1], *Zhe Su*[b,1,*], *Xuanye Tian*[a], *Guixiang Li*[b], *Kaili Zhang*[b,c], *Yi Luo*[b], *Bo Niu*[a,b], *Donghui Long*[a,b,*]

[a] Key Laboratory of Specially Functional Polymeric Materials and Related Technology (Ministry of Education), East China University of Science and Technology, Shanghai 200237, China.

[b] Structural Materials Research Department, Suzhou Laboratory, Suzhou 215000, China.

[c] School of Materials Science and Engineering, Harbin Institute of Technology, Harbin 150001, China.

[1] Co-first author. These authors contributed equally to this work

*Corresponding authors.

E-mail: philozhesu@163.com (Z. Su) and longdh@mail.ecust.edu.cn (D. Long).

Part A: Equations

According to the transmission line theory, the values of RL are calculated via the following equations:[1,2]

$$RL(dB) = 20log\left|\frac{Z_{in} - Z_0}{Z_{in} + Z_0}\right| \quad \text{(Equation S1)}$$

$$Z_{in} = Z_0\sqrt{\frac{\mu_r}{\varepsilon_r}}\tanh\left|j\left(\frac{2\pi fd}{c}\right)\right|\sqrt{\varepsilon_r\mu_r} \quad \text{(Equation S2)}$$

where Z_0 is the impedance of free space, Zin is the normalized input impedance of the absorber, ε_r ($\varepsilon_r = \varepsilon' - j\varepsilon''$) is the relative complex permittivity of the absorber, μ_r ($\mu_r = \mu' - j\mu''$) is the relative complex permeability, f represents the electromagnetic wave frequency, c is the velocity of the EMW in free space, and d expresses the thickness of the absorber, respectively.

Debye dipolar relaxation (Cole-Cole model), where the permittivity can be described as:[3]

$$\varepsilon_r = \varepsilon' - j\varepsilon'' = \varepsilon_\infty + \frac{\varepsilon_s - \varepsilon_\infty}{1 + j2\pi f\tau} \quad \text{(Equation S3)}$$

where τ, ε_s, ε_∞, and f stands for the polarization relaxation time, static permittivity constant, relative dielectric permittivity at the infinite frequency, and frequency, respectively. The ε' and ε'' can be deduced as follows:[4]

$$\varepsilon' = \varepsilon_\infty + \frac{\varepsilon_s - \varepsilon_\infty}{1 + (2\pi f\tau)^2} \quad \text{(Equation S4)}$$

$$\varepsilon'' = \varepsilon_\infty + \frac{2\pi f\tau(\varepsilon_s - \varepsilon_\infty)}{1 + (2\pi f\tau)^2} \quad \text{(Equation S5)}$$

Based on above equations, the relationship between ε' and ε'' can be written as:

$$\left(\varepsilon^{'}-\frac{\varepsilon_s+\varepsilon_\infty}{2}\right)^2+\left(\varepsilon^{''}\right)^2=\left(\frac{\varepsilon_s-\varepsilon_\infty}{2}\right)^2 \quad \text{(Equation S6)}$$

The eddy current can be calculated by the following eddy equation:[5]

$$C_0=\mu^{''}\left(\mu^{'}\right)^{-2}(f)^{-1}=2\pi\mu_0 d^2\sigma/3 \quad \text{(Equation S7)}$$

where μ_0 and σ are the permeability of vacuum and the electric conductivity, respectively.

The attenuation constant α determines the dissipation properties of the material. It can be evaluated through the following equation:[6]

$$\alpha=\frac{\sqrt{2}\pi f}{c}\times\sqrt{\left(\varepsilon^{''}\mu^{''}-\varepsilon^{'}\mu^{'}\right)+\sqrt{\left(\varepsilon^{''}\mu^{''}-\varepsilon^{'}\mu^{'}\right)^2+\left(\varepsilon^{''}\mu^{'}+\varepsilon^{'}\mu^{''}\right)^2}} \quad \text{(Equation S8)}$$

Delta values ($|\Delta|$) can be deduced by the following equations:

$$|\Delta|=\left|\sinh^2(Kfd)-M\right| \quad \text{(Equation S9)}$$

where K and M can be determined by the relative complex permittivity and permeability via following equations:[7]

$$K=\frac{4\pi\sqrt{\varepsilon^{'}\mu^{'}}\cdot\sin\frac{\delta_\varepsilon+\delta_\mu}{2}}{c\cdot\cos\delta_\varepsilon\cdot\cos\delta_\mu} \quad \text{(Equation S10)}$$

$$M=\frac{4\mu^{'}\varepsilon^{'}\cos\delta_\varepsilon\cos\delta_\mu}{\left(\mu^{'}\cos\delta_\varepsilon-\varepsilon^{'}\cos\delta_\mu\right)^2+\left[tan\left(\frac{\delta_\mu-\delta_\varepsilon}{2}\right)\right]^2\left(\mu^{'}\cos\delta_\varepsilon+\varepsilon^{'}\cos\delta_\mu\right)^2} \quad \text{(Equation S11)}$$

The normalized input impedance (Z) can be calculated by the following equation:

$$Z=\sqrt{\frac{\mu_r}{\varepsilon_r}}tanh\left(\frac{2\pi fd}{c}j\times\sqrt{\varepsilon_r\cdot\mu_r}\right) \quad \text{(Equation S12)}$$

Part B: Density functional theory (DFT) calculation

All density functional theory (DFT) calculations were performed using the Vienna Ab initio Simulation Package (VASP), within the framework of the generalized gradient approximation (GGA) with the Perdew-Burke-Ernzerhof (PBE) exchange-correlation functional. Projected augmented wave (PAW) potentials were adopted to describe the ionic cores, while valence electrons were represented by a plane wave basis set with a kinetic energy cutoff of 450 eV. Gaussian smearing (σ = 0.05 eV) was employed to handle the partial occupancies of Kohn−Sham orbitals. For the joint optimization of geometry and lattice parameters, Brillouin zone integration was carried out using a Monkhorst-Pack k-point mesh with a grid density of 0.04 $Å^{-1}$. Self-consistent field (SCF) calculations were converged to an energy threshold of 10^{-5} eV, whereas a stricter convergence criterion of 10^{-6} eV was applied for density of states (DOS) calculations. The equilibrium geometries and lattice constants were optimized until the maximum residual force on each atom was reduced to 0.02 $eV \cdot Å^{-1}$. A 15 Å vacuum layer was added perpendicular to the surface to eliminate spurious interactions between periodic images. Grimme's DFT-D3 dispersion correction was incorporated to account for weak van der Waals interactions. Spin polarization was enabled to accurately describe the magnetic properties of the system. Additionally, Bader charge analysis was performed using the Bader Charge Analysis code to quantify the charge transfer behavior.

Part C: Figures and Tables

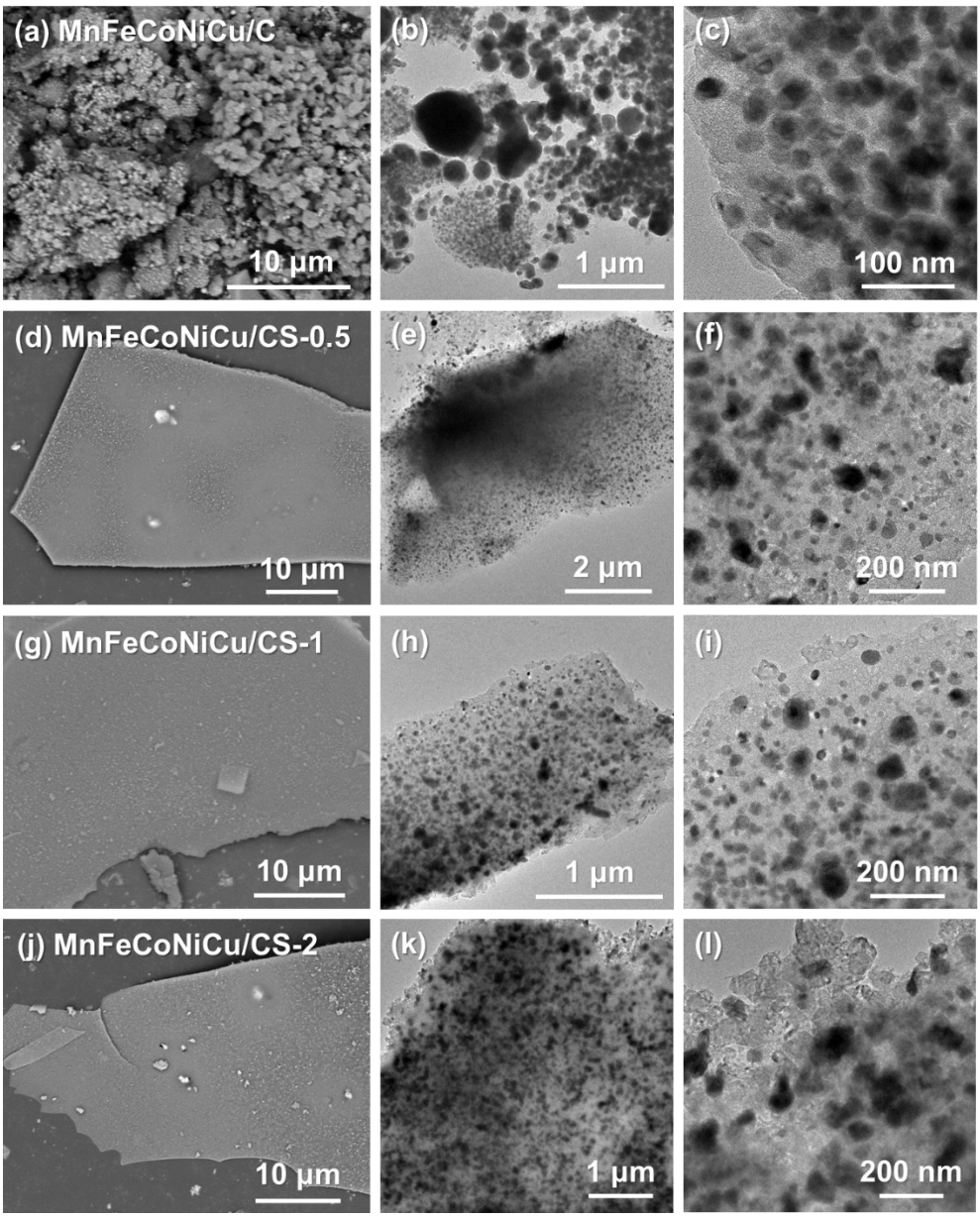

Fig.S1 (a,d,g,j)SEM images and (b,c,e,f,h,I,k,l) TEM images of all samples.

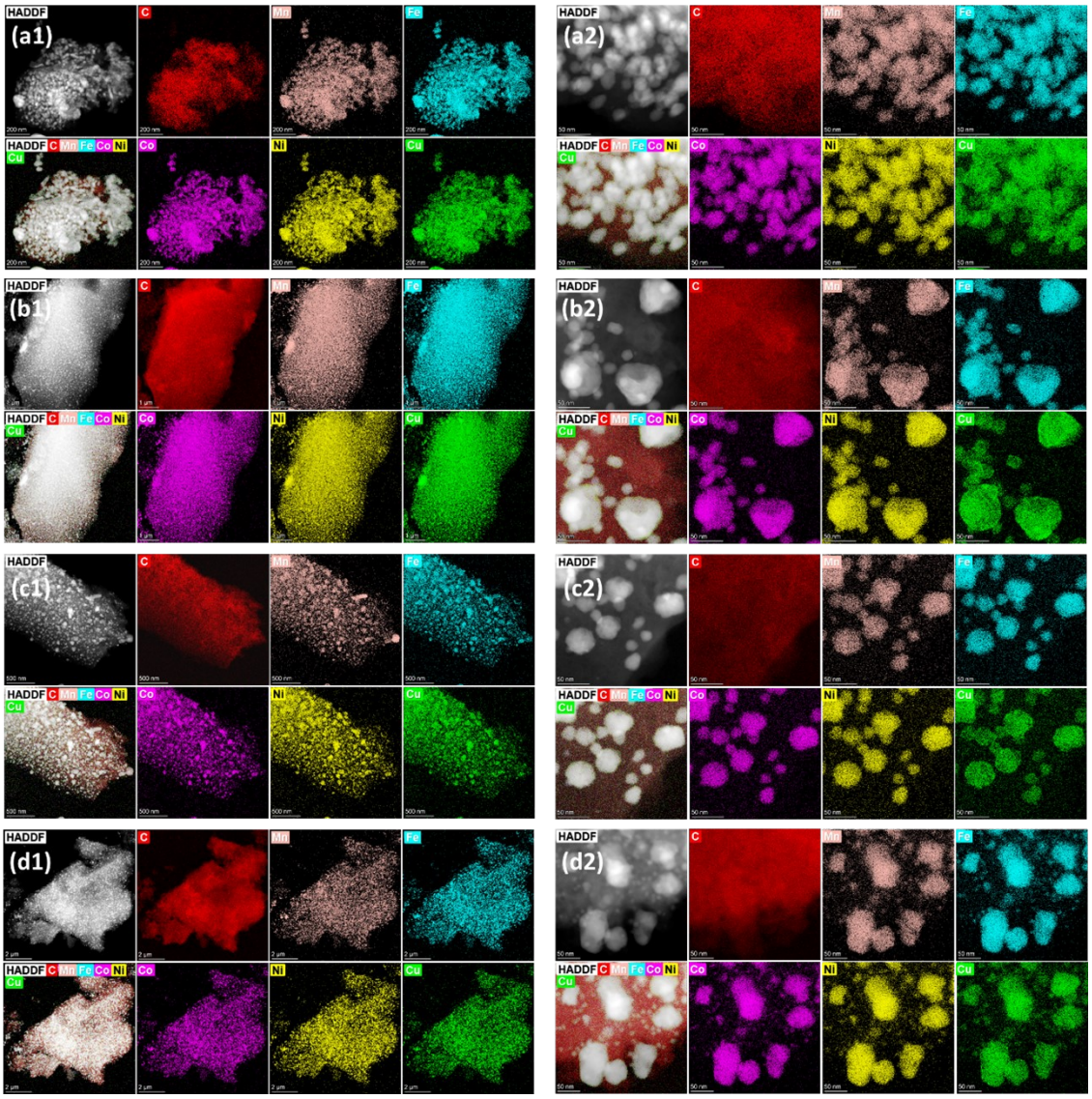

Fig.S2 EDS elements mapping images of all composites: (a) MnFeCoNiCu/C, (b) MnFeCoNiCu/CS-0.5, (c) MnFeCoNiCu/CS-1 and (d) MnFeCoNiCu/CS-2. (1-High-resoulation images, 2-Low-resolution images)

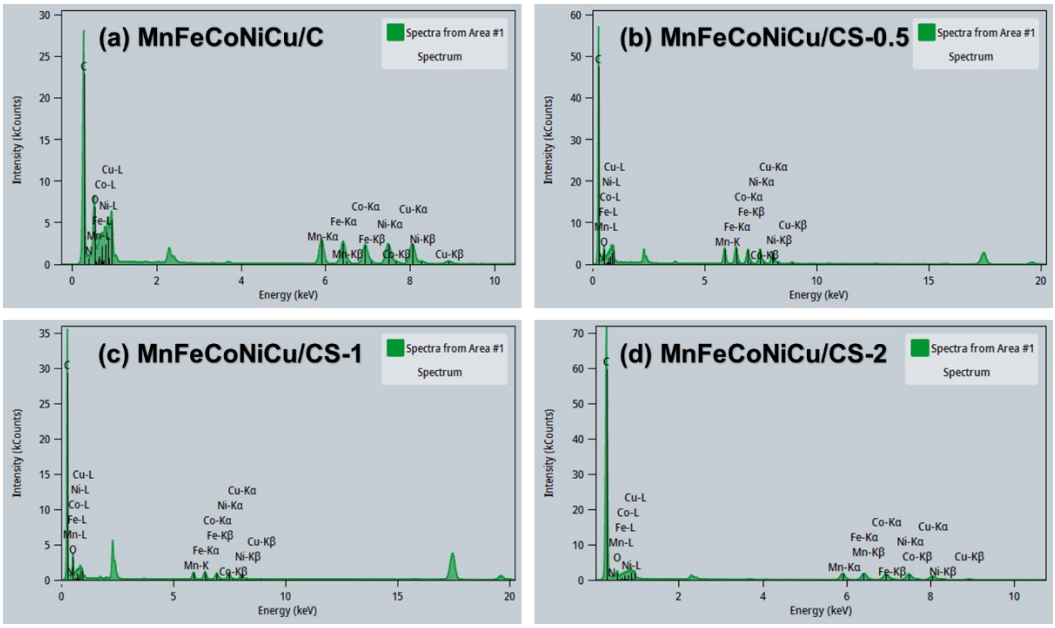

Fig.S3 EDS energy spectrum of (a) MnFeCoNiCu/C, (b) MnFeCoNiCu/CS-0.5, (c) MnFeCoNiCu/CS-1, and (d) MnFeCoNiCu/CS-2

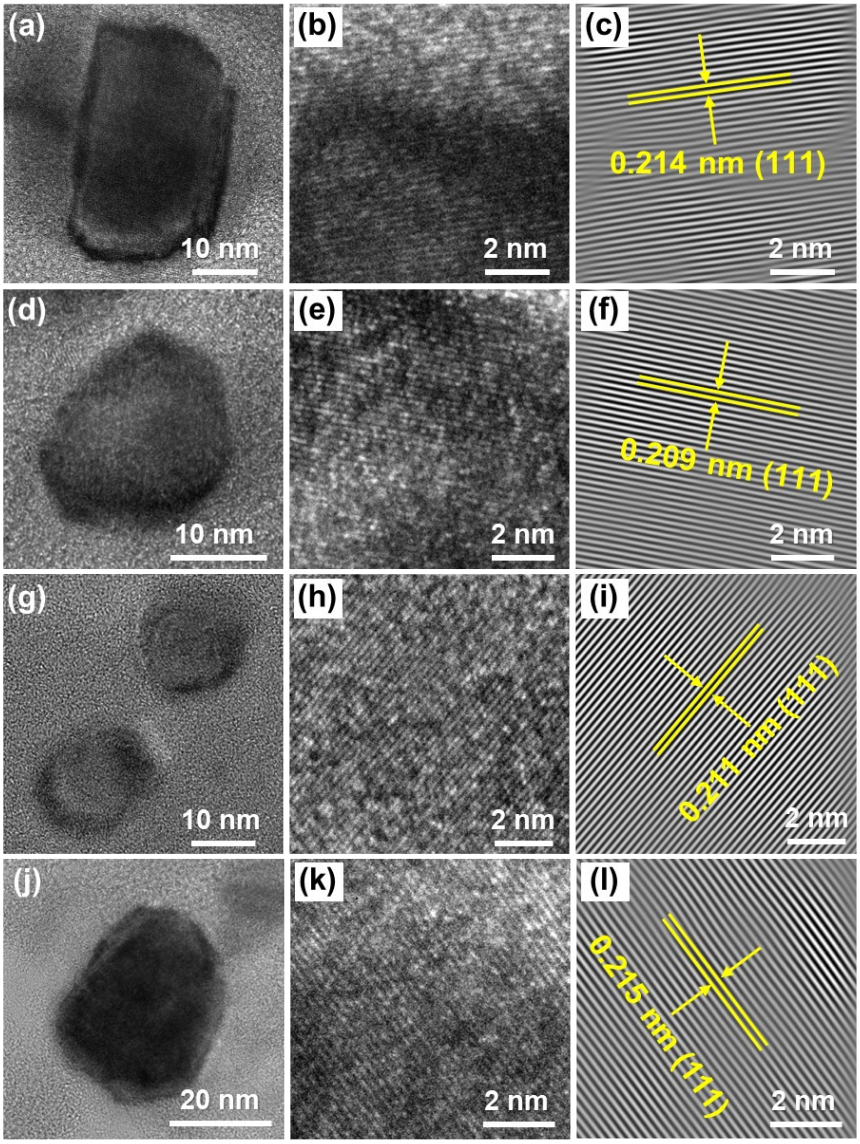

Fig.S4 HRTEM image and lattice image after inverse Fourier transform of (a-c) MnFeCoNiCu/C, (d-f) MnFeCoNiCu/CS-0.5, (g-i) MnFeCoNiCu/CS-1 and (j-l) MnFeCoNiCu/CS-2 respectively.

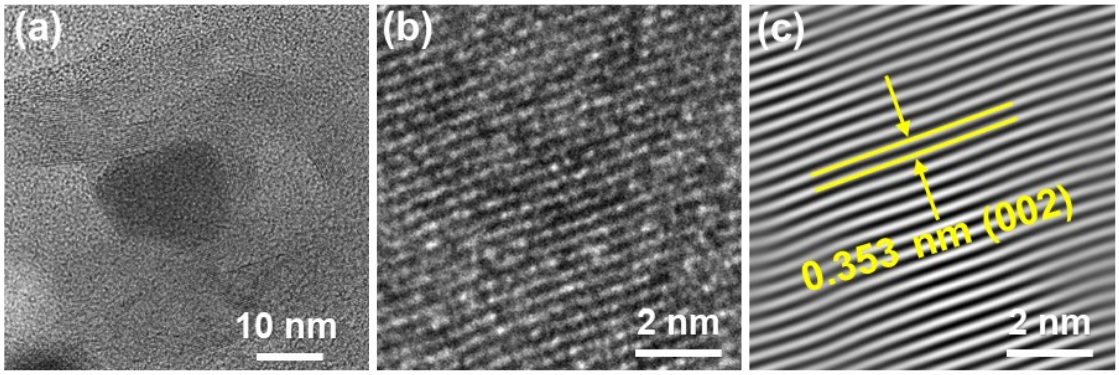

Fig.S5 (a) TEM image, (b) HRTEM image and (c) lattice image after inverse Fourier transform of onion-like graphitized carbon structure in MnFeCoNiCu/CS-1.

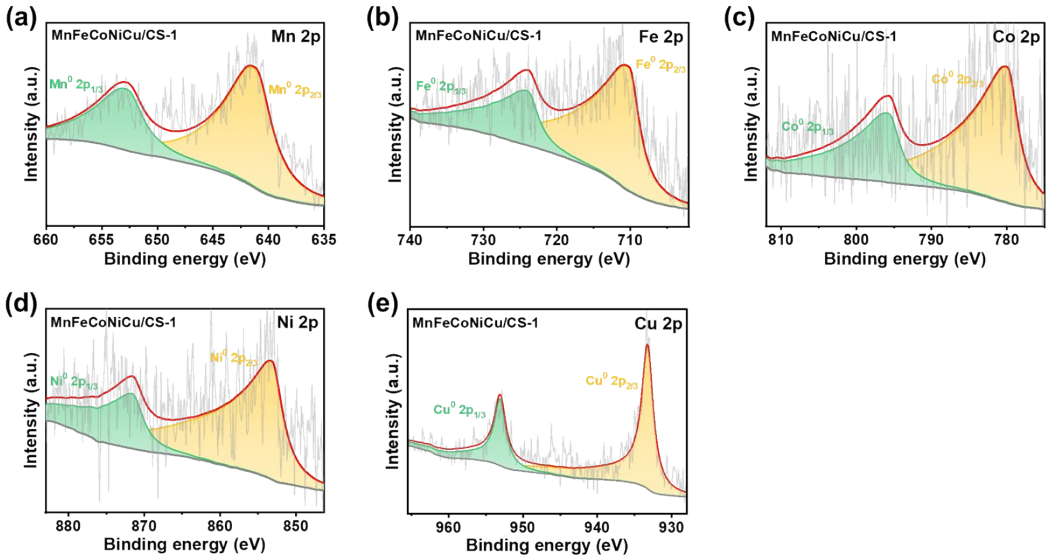

Fig.S6 High-resolution (a)Mn 2p, (b) Fe 2p, (c) Co 2p, (d) Ni 2p and (e) Cu 2p XPS spectra of MnFeCoNiCu/CS.

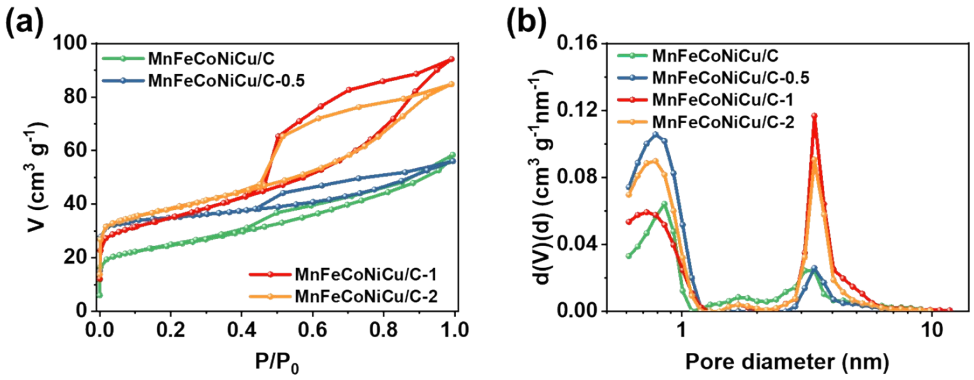

Fig.S7 (a) N2 absorption/desorption isotherms and (b) corresponding pore-size distribution curves of all samples.

MnFeCoNiCu/CS-1 and MnFeCoNiCu/CS-2 exhibit significant hysteresis loops within a relatively high range of relative pressure (P/P_0 = 0.4-0.99), demonstrating their abundance mesopores structure. The corresponding QSDFT pore distribution curve shows two pore size distributions within the range of micropores (0.6-1.1 nm) and mesopores (2-6 nm). The BET surface areas of MnFeCoNiCu/C, MnFeCoNiCu/CS-0.5, MnFeCoNiCu/CS-1 and MnFeCoNiCu/CS-2 gradually increased to 87, 120, 122 and 137 m^2/g, respectively (Table.S3).

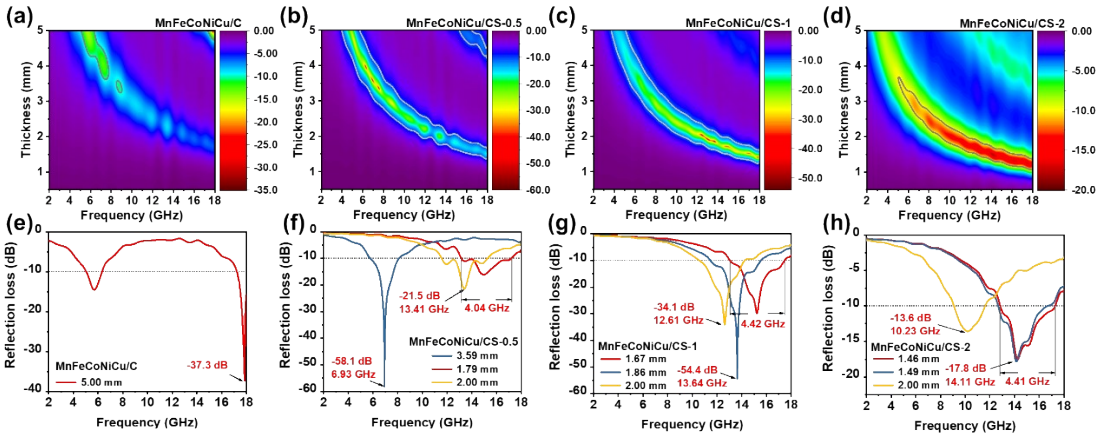

Fig.S8 (a-d) The reflection loss contour plot and (e-h) reflection loss curves at given thickness of all composites.

Note: relationship between matching thickness and absorption performance

The matching thickness follows the quarter-wavelength cancellation condition:

$$t_m = \frac{n\lambda}{4} = \frac{nc}{4f_m\sqrt{\varepsilon_r\mu_r}} (n = 1,3,5,\ldots)$$

In our work, the optimal matching thickness for MnFeCoNiCu/CS-1 is 1.86 mm, which satisfies the quarter-wavelength condition. Thinner thicknesses (e.g., 1.67 mm) give a wider EAB (4.42 GHz) but slightly higher RL value. We have added a contour plot of RL as a function of thickness and frequency for all composites in Fig. S8 to visually show how the minimum RL shifts with thickness. The relationship can be summarized as follows: The absorption peak shifts to lower frequencies as thickness increases. The EAB is maximized at an intermediate thickness. The RL_{min} occurs at the quarter-wavelength matching thickness.

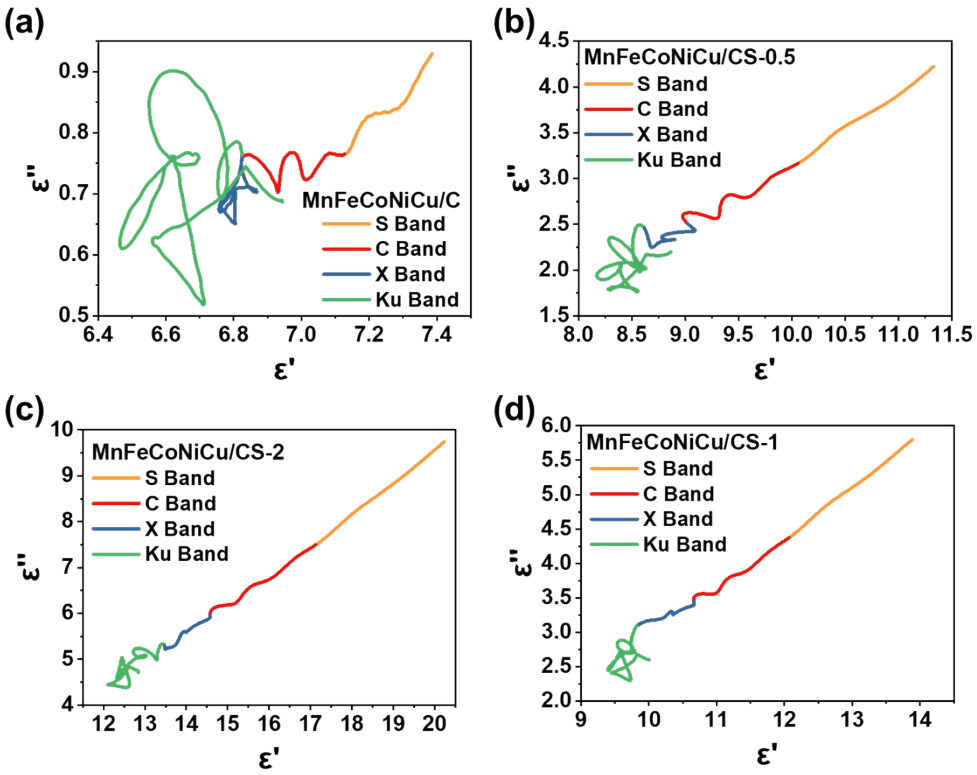

Fig.S9 The Cole-Cole plots of (a) MnFeCoNiCu/CS-0.5 and (b) MnFeCoNiCu/CS-2.

Table.S1 Detailed atomic ratio of the nano-alloys in MnFeCoNiCu/C, MnFeCoNiCu/CS-0.5, MnFeCoNiCu/CS-1, and MnFeCoNiCu/CS-2.

Sample	Atomic Fraction				
	Mn (%)	Fe (%)	Co (%)	Ni (%)	Cu (%)
MnFeCoNiCu/C	21.3	19.1	18.3	19.8	21.5
MnFeCoNiCu/CS-0.5	20.1	21.0	18.7	21.1	19.2
MnFeCoNiCu/CS-1	20.3	21.4	19.2	20.5	18.6
MnFeCoNiCu/CS-2	20.5	20.7	19.1	21.1	18.7

Table.S2 Detailed pore parameters of MnFeCoNiCu/C, MnFeCoNiCu/CS-0.5, MnFeCoNiCu/CS-1 and MnFeCoNiCu/CS-2.

Sample	S_{BET} (m^2/g)	S_{Micro} (m^2/g)	V_{Total} (cm^3/g)	V_{Micro} (cm^3/g)
MnFeCoNiCu/C	87	27	0.09	0.01
MnFeCoNiCu/CS-0.5	120	91	0.09	0.04
MnFeCoNiCu/CS-1	122	37	0.15	0.02
MnFeCoNiCu/CS-2	137	65	0.13	0.03

Table.S3 The intensity and area ratio in high-resolution C 1s XPS spectra

	Intensity	Integral area		Area ratio
	C-C	C-C	C-O	C-C/C-O
MnFeCoNiCu/C	108885	69220.3	21269.6	3.25
MnFeCoNiCu/CS-0.5	116095	77211.4	23180.5	3.33
MnFeCoNiCu/CS-1	151761	95311.5	28334.1	3.36
MnFeCoNiCu/CS-2	170350	105280.1	30696.6	3.43

Table.S4 Comparison of RL_{min} *versus* thickness and EAB *versus* frequency range among MnFeCoNiCu/CS-1 and other absorbers reported in the literature.

Sample	RL_{min} (dB)	Thickness (mm)	EAB (GHz)	Frequency range (GHz)	Reference
MnFeCoNiCu/CS-1	-54.4	1.86	4.42	13.05-17.47	This work
$FeCoNiCu_{0.5}Al$	-40.05	2.00	—	—	8
FeCoNiCrCu	-41.23	2.60	4.5	7.2-11.7	9
$FeCoNiCrCuAl_{0.3}$	-41.4	1.30	4.0	14.0-18.0	10
Co/CNFs	-45.0	1.80	4.6	12.7-17.3	11
MoS_2-C3	-41.90	1.20	3.0	14.0-17.0	12
CFs/silicone	-42.29	1.30	4.41	—	13
$ZnO/NiCo_2O_4$-7	-33.49	4.99	1.2	16.8-18.0	14
3D CoNi/N-GCT	-41.13	3.50	3.2	—	15
Si_3N_4-G-4	-26.7	3.25	4.2	8.2-12.4	16
GBS_2	-37.8	2.50	9.2	8.8-18.0	17
Fe_3GeTe_2	-34.7	5.50	2.24	9.0-11.24	18

Table.S5 Comparison of RL_{min} *versus* EAB among MnFeCoNiCu/CS-1 and other absorbers reported in the literature.

Sample	RL_{min} (dB)	EAB (mm)	Reference
MnFeCoNiCu/CS-1	-54.4	4.42	This work
FeCoNiCrCu	-41.23	4.5	9
$FeCoNiCrCuAl_{0.3}$	-41.40	4.0	10
Co/CNFs	-45.00	4.6	11
MoS_2-C3	-41.90	3.0	12
CFs/silicone	-42.29	4.41	13
3D CoNi/N-GCT	−41.13	3.2	15
Si_3N_4-G-4	−26.7	4.2	16
Fe_3GeTe_2	-34.70	2.24	18

Table.S6 Detailed average spin magnetic moments (μ_B) of each element for MnFeCoNiCu/CS-1.

Mn	Fe	Co	Ni	Cu
2.85	2.46	1.35	0.48	0.07

Table.S7 The conductivity of all composites.

Sample	Powder (S/m)	40 wt.% in paraffin (S/m)
MnFeCoNiCu/C	18.3	0.31
MnFeCoNiCu/CS-0.5	36.7	0.59
MnFeCoNiCu/CS-1	52.1	0.93
MnFeCoNiCu/CS-2	78.4	1.24

The complex permittivity is directly influenced by conductivity. According to Debye theory, the conductive loss is directly determined by the conductivity ($\varepsilon_c'' = \frac{\sigma}{2\pi f \varepsilon_0}$). However, high conductivity can cause severe impedance mismatch. MnFeCoNiCu/CS-2 has the highest conductivity and highest ε', its RL_{min} is only -17.8 dB. This is because the composites behave almost like a conductor, with most incident waves reflected at the surface rather than entering the absorber. MnFeCoNiCu/CS-1 achieves the best balance: sufficiently high conductivity for conductive loss, but not so high as to destroy impedance matching. MnFeCoNiCu/C has too low conductivity, resulting in weak dielectric loss and a larger matching thickness. Thus, an optimal conductivity window exists for our composites.

Reference

1 X. Zhang, Y. Zhang, J. He, H. Li, Y. Bai and S. Gao, *Fuel*, 2023, **331**, 125811, 10.1016/j.fuel.2022.125811.

2 Y. Liu, X. Zhou, Z. Jia, H. Wu and G. Wu, *Adv. Funct. Mater.*, 2022, **32**, 2204499, 10.1002/adfm.20220449.

3 L. Wang, M. Huang, X. Yu, W. You, B. Zhao, C. Liang, X. Liu, X. Zhang and R. Che, *J. Mater. Sci. Technol.*, 2022, **131**, 231-239, 10.1016/j.jmst.2022.05.015.

4 J. Yan, Y. Huang, Y. Yan, L. Ding, P. Liu, *ACS Appl. Mater. Interfaces*, 2019, **11**, 40781-40792, 10.1021/acsami.9b12850.

5 Z. Zou, M. Ning, Z. Lei, X. Zhuang, G. Tan, J. Hou, H. Xu, Q. Man, J. Li and R. Li, *Carbon*, 2022, **193**, 182-194, 10.1016/j.carbon.2022.03.017.

6 X. Zeng, X. Cheng, R. Yu and G.D. Stucky, *Carbon*, 2020, **168**, 606-623, 10.1016/j.carbon.2020.07.028.

7 Z. Lei, S. Li, A Zhang, Y. Song, N. He, M. Li, D. Geng, W. Liu, S. Ma and Z. Zhang, *Compos. Part B-eng.*, 2020, **234**, 109692, 10.1016/j.compositesb.2022.109692.

8 Y. Duan, L. Song, Y. Cui, H. Pang, X. Zhang and T. Wang, *J. Alloy. Compd.*, 2020, **848**, 156491, 10.1016/j.jallcom.2020.156491.

9 G. Li, H. Zhao, H. Wang, Z. Zhou, L. Gao, W. Su and C. Dong, *J. Alloy. Compd.*, 2023, **941**, 168822, 10.1016/j.jallcom.2023.168822.

10 H. Wu, D. Lan, B. Li, L. Zhang, Y. Fu, Y. Zhang and H. Xing, *Compos. Pt. B-Eng.*, 2019, **179**, 107524, 10.1016/j.compositesb.2019.107524.

11 J. Xu, N. Lu, Y. Zhao, L. Luo, M. Yuan, G. Sun, *Chem. Eng. J.*, 2024, **502**, 157870,

10.1016/j.cej.2024.157870.

12 J. Wang, Z. Wu, C. Yang, G. Chen, M. Yuan, B. Li, Y. Lai, R. Che, *Adv. Funct. Mater.*, 2024, **34**, 2409923, 10.1002/adfm.202409923.

13 Y. Liu, J. Zhou, Z. Ning, H. Huang, Z. Cheng, L. Duan, Y. Wang, X. Tao, P. Liu, Y. Ma, Z. Yao, *Adv. Funct. Mater.*, 2024, **34**, 2411573, 10.1002/adfm.202411573.

14 B. Du, M. Cai, X. Wang, J. Qian, C. He and A. Shui, *J. Adv. Ceram.*, 2021, **10**, 832-842, 10.1007/s40145-021-0476-z.

15 X. Zhang, X. Zhang, H. Yuan, K. Li, Q. Ouyang, C. Zhu, S. Zhang, Y. Chen, *Chem. Eng. J.*, 2019, **383**, 123208, 10.1016/j.cej.2019.123208.

16 F. Ye, Q. Song, Z. Zhang, W. Li, S. Zhang, X. Yin, Y. Zhou, H. Tao, Y. Liu, L. Cheng, L. Zhang and H. Li, *Adv. Funct. Mater.*, 2018, **28**, 1707205, 10.1002/adfm.201707205.

17 X. You, H. Ouyang, R. Deng, Q. Zhang, Z. Xing, X. Chen, Q. Shan, J. Yang and S. Dong, *Nano-Micro Lett.*, 2025, **17**, 27, 10.1007/s40820-024-01541-y.

18 G. Li, S. Ma, Z. Li, Y. Zhang, J. Diao, L. Xia, Z. Zhang and Y. Huang, *ACS Nano*, 2020, **16**, 7861-7879, 10.1021/acsnano.2c00512.